The Astronomical Journal, 162:269 (11pp), 2021 December https://doi.org/10.3847/1538-3881/ac2a2c

Reinvestigation of the Multiepoch Direct Detections of HD 88133 b and Upsilon Andromedae b

Cam Buzard[1], Danielle Piskorz[2], Alexandra C. Lockwood[3], Geoffrey Blake[1,2], Travis S. Barman[4], Björn Benneke[5], Chad F. Bender[6], and John S. Carr[7]
[1] Division of Chemistry and Chemical Engineering, California Institute of Technology, Pasadena, CA 91125, USA; cbuzard@caltech.edu
[2] Division of Geological and Planetary Sciences, California Institute of Technology, Pasadena, CA 91125, USA
[3] Space Telescope Science Institute, Baltimore, MD 21218, USA
[4] Lunar and Planetary Laboratory, University of Arizona, Tuscon, AZ 85721, USA
[5] Institute for Research on Exoplanets, University of Montreal, Montreal, QC, Canada
[6] Department of Astronomy and Steward Observatory, University of Arizona, Tuscon, AZ 85721, USA
[7] Department of Astronomy, University of Maryland, College Park, MD 20742, USA
Received 2021 July 19; revised 2021 September 9; accepted 2021 September 24; published 2021 November 29

Abstract

We reanalyze the multiepoch direct detections of HD 88133 b and ups And b that were published in Piskorz et al. (2016) and Piskorz et al. (2017), respectively. Using simulations to attempt to reproduce the detections, we find that with the six and seven *L*-band Keck/NIRSPEC epochs analyzed in the original works, the planets would not have been detectable unless they had unreasonably large radii. HD88133 and ups And both have fairly large stellar radii, which contributed to the difficulty in detecting the planets. We take this opportunity to consider how these planets may have been detectable with the small number of epochs originally presented by running simulations both with the upgraded NIRSPEC instrument and with near-zero primary velocities, as recommended by Buzard et al. (2021). While seven *L*-band NIRSPEC2.0 epochs with near-zero primary velocities would have allowed a strong (10.8σ) detection of ups And b, many more than six *L*-band epochs would have been required for a strong detection of HD88133b, which could be due in part to both this system's large stellar radius and low stellar temperature. This work stresses the importance of careful analytic procedures and the usefulness of simulations in understanding the expected sensitivity of high-resolution spectroscopic data.

Unified Astronomy Thesaurus concepts: High resolution spectroscopy (2096); Radial velocity (1332); Exoplanets (498)

1. Introduction

Direct detection techniques that use radial-velocity signatures from exoplanet orbital motion to detect their atmospheric thermal emission have become popular in the last decade. Two variations of such high-resolution techniques have been developed. Both aim to make a direct planetary detection through a measurement of the planetary-velocity semiamplitude, K_p. One variation targets planetary systems during periods when the change in the planetary line-of-sight motion is the greatest, typically near conjunction. By observing the system at periods of maximum planetary line-of-sight acceleration, the data contain planetary signatures that shift across the instrument's resolution elements over the course of the night, and techniques like principal component analysis (PCA) can be used to tease apart the changing planetary signal and the stationary telluric and stellar signals. A one-dimensional cross-correlation routine can then be used to measure the planetary velocity. This technique was first introduced by Snellen et al. (2010) with VLT/CRIRES, and has since been applied to data from a range of instruments including Subaru/HDS (e.g., Nugroho et al. 2017), TNG/GIANO (e.g., Brogi et al. 2018; Guilluy et al. 2019), and CFHT/SPIRou (e.g., Pelletier et al. 2021).

The second variation of the high-resolution technique, which is the focus of this work, instead limits observations so that the change in the planetary line-of-sight velocity is minimized, and the planetary spectrum does not shift across the detector during the course of an observation. This variation is more technically challenging because there is no longer a velocity variation that can be leveraged to separate the planetary and stellar spectra in a single epoch. After the data is telluric corrected, a two-dimensional cross correlation is relied upon to pull apart the stellar and planetary components. Since the planetary signal is so much fainter than the stellar signal, multiple epochs must be combined before the planetary signal becomes apparent. While technically challenging, this variation is the only currently viable high-resolution method for studying the atmospheres of planets whose semimajor axes preclude both single epoch spectroscopic detection, because they move too slowly, and direct imaging with current adaptive optics capabilities, because they are too close to the star ($\lesssim 0.1''$; e.g., Snellen et al. 2014). This gap includes planets in K-dwarf and solar habitable zones. As the so-called multiepoch technique is uniquely capable of directly studying the atmospheres of nontransiting planets in these systems, it deserves careful work and attention.

To date, the multiepoch technique has mainly been applied to data from Keck/NIRSPEC, which is an echelle spectrograph that offered 4–6 orders in the *K* and *L* bands per cross disperser setting and $R \sim 25{,}000$–$30{,}000$ before its upgrade in early 2019. The method was first applied to Tau Boötis b and was able to measure its K_p as $111 \pm 5\ \mathrm{km\ s^{-1}}$

(Lockwood et al. 2014), which was in good agreement with K_p measurements from other techniques (e.g., $110.0 \pm 3.2\,\mathrm{km\,s^{-1}}$, Brogi et al. 2012). Subsequently, the nontransiting hot-Jupiter HD 88133 b and Upsilon Andromedae b (ups And b) were detected at $40 \pm 15\,\mathrm{km\,s^{-1}}$ (Piskorz et al. 2016) and $55 \pm 9\,\mathrm{km\,s^{-1}}$ (Piskorz et al. 2017), respectively. These planets have yet to be studied via a different technique. Piskorz et al. (2018) then detected the transiting hot-Jupiter KELT-2Ab with a K_p of $148 \pm 7\,\mathrm{km\,s^{-1}}$, which was in good agreement with the transit measurement of $145^{+9}_{-8}\,\mathrm{km\,s^{-1}}$ (Beatty et al. 2012). Finally, Buzard et al. (2020) measured K_p of the nontransiting hot-Jupiter HD 187123 b to be $53 \pm 13\,\mathrm{km\,s^{-1}}$. This detection used simulations to identify sources of nonrandom noise and elucidate the true planetary detection. HD 187123 b has not to date been detected via another technique.

In this work, we look back on the multiepoch detections of HD 88133 b (Piskorz et al. 2016) and ups And b (Piskorz et al. 2017). Piskorz et al. (2016) reported the Keplerian orbital velocity of HD 88133 b as $40 \pm 15\,\mathrm{km\,s^{-1}}$ using six epochs of NIRSPEC L-band data and three epochs of K-band data. Piskorz et al. (2017) reported the Keplerian orbital velocity of ups And b as $55 \pm 9\,\mathrm{km\,s^{-1}}$ using seven epochs of NIRSPEC L-band data, three epochs of K_l-band data covering the left-hand half of the NIRSPEC detector, and three epochs of K_r band data covering the right-hand half of the detector. In this work, we will focus on the L-band data because the L-band data provided the majority of the overall structure in both the HD 88133 b and ups And b detections.

2. Standard Multiepoch Analytic Approach

To begin, we want to give a brief description of the multiepoch analytic process. These approaches are explained in more detail in prior publications (e.g., Lockwood et al. 2014; Piskorz et al. 2016; Buzard et al. 2020). In brief, epochs of data are obtained from hot-Jupiter systems over ~2–3 hr periods during which the planetary signal is not expected to significantly shift compared to the wavelength scale of the detector. The two-dimensional echelle spectra are reduced, wavelength calibrated, telluric corrected, and run through a two-dimensional cross-correlation routine with appropriate stellar and planetary spectral models. Because the stellar signal is the major component of the data after telluric correction, the known stellar velocity, given by

$$v_{\mathrm{pri}} = v_{\mathrm{sys}} - v_{\mathrm{bary}} \tag{1}$$

where v_{sys} is the systemic velocity and v_{bary} is the barycentric velocity, can always be correctly measured in each epoch. A cut along the known stellar velocity gives a one-dimensional cross correlation in terms of planetary velocity shift. With a very low contrast relative to the stellar signal, the planetary signal requires the combination of multiple epochs to become clearly detectable.

To be combined, the cross correlations must first undergo two transitions. They must first be converted from functions of secondary velocity, which is dependent on orbital phase, to functions of a parameter independent of orbital phase; namely, the Keplerian orbital velocity. Second, they must be converted to log likelihoods. To convert them from functions of secondary velocity to Keplerian orbital velocity (K_p), we apply the equation,

$$v_{\mathrm{sec}}(f) = -K_p(\cos(f + \omega_{\mathrm{st}}) + e\cos(\omega_{\mathrm{st}})) + v_{\mathrm{pri}} \tag{2}$$

where f is the planet's true anomaly at the observation time, ω_{st} is the argument of periastron of the star's orbit measured from the ascending node (with the Z-axis pointing away from the observer, see Fulton et al. 2018), and e is the eccentricity.

To convert the cross correlations from v_{sec} to K_p space using Equation (2), we need stellar radial-velocity (RV) parameters (e, ω_{st}) and true anomaly (f) values at each epoch. Stellar RV parameters can typically be found in the literature (e.g., Butler et al. 2006). We note that it is important that the stellar orbital parameters (e, ω_{st}) as well as those used to calculate f (t_{peri}, P) are pulled from the same literature source. This will be especially important for near-circular orbits where pericenter is not well defined because though references can set pericenter at vastly different points on the orbit, their other parameters (mainly t_{peri} and ω) would then all be consistent to that chosen point of pericenter. A t_{peri} and ω from different references could be referring to very different points on the orbit, and so could create a large error in the derived fs and secondary velocities.

The true anomalies can be calculated using the following equations, which are described in Murray & Dermott (1999). First, the mean anomaly (M) is calculated from the observation time (t_{obs}), the stellar RV parameters: time of periastron (t_{peri}) and orbital period (P). If the orbit under study can be assumed circular, the mean anomalies can be used in place of the true anomalies.

$$M = 2\pi\left(\frac{t_{\mathrm{obs}} - t_{\mathrm{peri}} \bmod P}{P}\right). \tag{3}$$

Then, the eccentric anomaly E can be calculated as follows, where e is the eccentricity. As this equation does not have a closed-form solution for E given M, E is calculated numerically.

$$M = E - e\sin E. \tag{4}$$

Finally, the true anomaly f is calculated as

$$f = 2\arctan\left(\sqrt{\frac{1+e}{1-e}}\tan\frac{E}{2}\right). \tag{5}$$

We want to make a few important notes about Equations (2) and (3)–(5). First, the negative sign at the start of Equation (2), which is not present in the corresponding equation in Fulton et al. (2018), allows this equation to describe the planetary motion, rather than the stellar motion. At any given time, the planetary and stellar motions should have opposite signs. The addition of the negative sign would be equivalent to replacing ω_{st} with ω_{pl} (the argument of periastron of the planet's orbit measured from the ascending node) because $\omega_{\mathrm{pl}} = \omega_{\mathrm{st}} + \pi$ (for a set direction of the Z axis). Importantly, by defining K_p this way, we specify that it must be a positive value. Second, it is important that the zero point used to define the anomalies (t_{peri} in Equation (3)) is consistent with the offset used in Equation (2). In the equations as written, f is measured from pericenter, and adding ω_{st} in Equation (2) brings the zero point from pericenter to the star's ascending node. The ascending node (for a circular orbit, when the star is at quadrature and moving away from the observer or when the planet is at quadrature and moving toward the observer) should have the largest negative v_{sec} possible. The negative cosine ensures this

is the case. Other works that have assumed a circular orbit (e.g., Piskorz et al. 2018; Buzard et al. 2020) use a positive sine equation with no added phase offset and with Ms centered at inferior conjunction. This is also a valid approach because the offset between the Ms and the sine equation are consistent.

Once the planetary cross correlations from different epochs are on the same K_p axis, they must be converted into log likelihoods to be combined. There are a number of ways to do so (Zucker 2003; Brogi & Line 2019; Buzard et al. 2020). Here, we use the approach first introduced by Zucker (2003) and termed the "Zucker ML" approach by Buzard et al. (2020) to be consistent with Piskorz et al. (2016) and Piskorz et al. (2017). The Zucker ML method converts cross correlations to log likelihoods and combines them as,

$$\log(L(s)) = \sqrt{1 - \exp\left(\frac{1}{N_{\rm tot}}\Sigma_i N_i \log[1 - R_i^2(s)]\right)}, \quad (6)$$

where s is the velocity shift, R_i are the individual cross correlations, N_i is the number of pixels per cross correlation, and $N_{\rm tot}$ is the total number of pixels.

With this basis, we turn to a reinvestigation of previous multiepoch works by Piskorz et al. (2016) and Piskorz et al. (2017).

3. HD 88133 B

Piskorz et al. (2016) used six Keck/NIRSPEC L-band and three K-band epochs to measure the planetary Keplerian orbital velocity of the nontransiting hot-Jupiter HD 88133 b as $40 \pm 15\,{\rm km\,s^{-1}}$. To do so, they used orbital parameters from their own fit to stellar RV data. This stellar RV data set consisted of 55 RV points; 17 had been previously analyzed by Fischer et al. (2005) and the rest were new RV points taken by the California Planet Survey with HIRES at the W. M. Keck Observatory. Fitting these data with a Markov chain Monte Carlo technique following Bryan et al. (2016), they reported the orbital parameters (velocity semiamplitude $K = 32.9 \pm 1.03\,{\rm km\,s^{-1}}$, period $P = 3.4148674^{+4.57e-05}_{-4.73e-05}$ days, eccentricity $e = 0.05 \pm 0.03$, argument of periastron of the star's orbit $\omega_{\rm st} = 7.22^{+31.39\circ}_{-48.11}$, and time of periastron $t_{\rm peri} = 2454641.984^{+0.293}_{-0.451}$).

3.1. Correction to Piskorz et al. (2016) Results

In Piskorz et al. (2016) there was a systematic error in the implementation of the time of periastron in Equation (3) that resulted in a 38.0% orbital offset in the mean anomalies. The anomalies used in the paper analysis and the corrected anomalies are listed in Table 1.

In Figure 1, we show the corrected log-likelihood curves along with the originally published curves, analyzed with both the SCARLET and the PHOENIX planetary models. This correction causes a drastic difference in the resulting log-likelihood curve. In each subplot, the red curve was the published log(L) curve and the black dashed curve is the curve reproduced with the systematic offset. Interestingly, this curve exactly reproduces the SCARLET model function, but does not reproduce the PHOENIX model function. In fact, when the data are analyzed with the PHOENIX model, Piskorz et al. (2016) orbital parameters, and the offset, the resulting function appears much more similar in shape to the corresponding SCARLET result than was originally published in Piskorz et al. (2016). This suggests that the two planetary models are much more comparable than was originally thought.

Table 1
HD 88133 b Epoch Positions

Date	Piskorz et al. (2016)		This work	
	M[a]	f[a]	M	f
2012 Apr 1	5.11	5.01	1.22	1.31
2012 Apr 3	2.51	2.57	4.90	4.80
2013 Mar 10	1.52	1.62	3.91	3.84
2013 Mar 29	4.95	4.85	1.06	1.15
2014 May 14	1.03	1.12	3.42	3.40
2015 Apr 8	3.26	3.25	5.65	5.59

Note.
[a] Note, the values here are expressed from 0 to 2π, rather than from 0 to 1 as in Piskorz et al. (2016). The M and f values reported in their Table 3 also differ from these values because while they too were affected by the systematic offset, they used Butler et al. (2006) orbital parameters rather than the newly fit parameters from Piskorz et al. (2016).

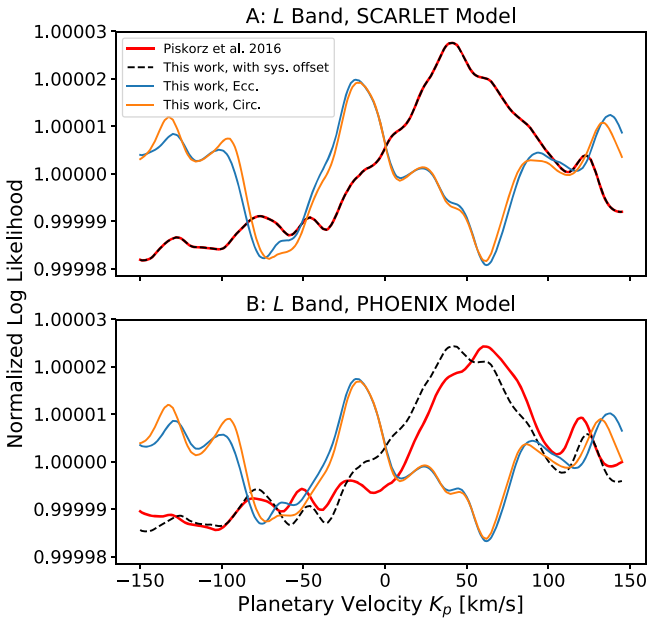

Figure 1. (A) The normalized log-likelihood result for HD 88133 b originally published in Piskorz et al. (2016) is shown in red. The black dashed curve is able to reproduce the published curve by including a systematic offset in epoch positions. In blue and orange are the corrected log-likelihood curves considering an eccentric orbit (blue) and a circular orbit (orange). (B) Same as panel A, except using a PHOENIX planetary model rather than a SCARLET planetary model. Note here that we were unable to reproduce the published curve. However, when the same orbital parameters are used, we get a much more similar result to that of the SCARLET models than was shown in the Piskorz et al. (2016). The two different planetary spectral-model frameworks do not create as significant a difference as we thought.

The blue and orange curves in both subplots show the corrected log likelihoods when the orbit is either treated as eccentric (blue) or assumed to be circular (orange). The similarity between these curves in both subplots shows that for low eccentricity orbits (here $e \sim 0.05$) circular approximations do not greatly affect the shape of the resulting log-likelihood surface.

We also note that when the corrected log-likelihood curves show no significant peaks at positive values of K_p. Remember that given how we defined the relationship between $v_{\rm sec}$ and K_p, only positive values of K_p are physically meaningful. Negative

values of K_p would have the stellar and planetary RV curves perfectly in phase rather than out of phase as they should be. This correction therefore implies that we cannot report a measurement of the Keplerian orbital velocity of HD88133b of 40 km s^{-1} from the six L-band epochs presented in Piskorz et al. (2016).

3.2. HD88133 Simulations

We ran a few sets of simulations to determine what physical or observational factors would allow for the detection of HD88133b. We note that HD88133A has a rather large stellar radius of 2.20 $R_\odot$ (Ment et al. 2018), meaning that this system has an even lower planet-to-star contrast than most hot Jupiters, though we cannot measure it directly because of the unknown planetary radius. Our first simulations ask how large the planetary radius would have to be for the planetary peak to be detectable in the six L-band epoch observed (Section 3.2.2). Next, we investigate whether the same epochs taken with the upgraded NIRSPEC2.0 instrument would have been more successful than the NIRSPEC1.0 epochs (Section 3.2.3). Then, we consider the primary velocity. Buzard et al. (2021) found that epochs with near-zero primary velocities were more useful in damping down structured noise and revealing true planetary signatures than epochs with larger absolute primary velocities. We consider whether the observed epochs would have better revealed the planetary peak if they had smaller absolute primary velocities (Section 3.2.4).

3.2.1. Generation of Simulated Data

For these simulations, we use a stellar model generated from the PHOENIX stellar spectral-model grid (Husser et al. 2013) interpolated to an effective temperature of 5438 K, a metallicity of 0.330, and a surface gravity of 3.94 (Mortier et al. 2013).

We use the PHOENIX planetary spectral model from Piskorz et al. (2016). This modeled atmosphere does not have an inverted thermal structure in regions close to the molecular photosphere.

We generated the simulated multiepoch data using the same framework initially presented in Buzard et al. (2020) and so a full description can be found there. As a quick summary, these simulations combine the stellar and planetary models on the planetary wavelength axis after scaling them by their relative surface areas and shifting them to the desired primary and secondary velocities during each epoch. The secondary velocities are calculated by plugging the "This work" f values from Table 1 into Equation (2) with Piskorz et al. (2016) orbital parameters and a K_p of 40 km s^{-1}. For these simulations, we assume a planetary radius of 1 $R_{\rm Jup}$ (except in the planetary radius simulations) and a stellar radius of 2.20 $R_\odot$ (Ment et al. 2018). After combination, the continuum is removed using a third-order polynomial fit from 2.8 to 4.0 μm in wavenumber space. Then, the simulated data are broadened using the instrumental profiles fit to the data, interpolated onto the data wavelength axes, and the same pixels lost to saturated tellurics in the data are removed. The data, all taken before the NIRSPEC upgrade in early 2019, contain four orders per epoch, which cover approximately 3.4038–3.4565, 3.2567–3.3069, 3.1216–3.1698, and 2.997–3.044 μm. Gaussian white noise is added in at the same level as in the data (total S/N per pixel = 5352).

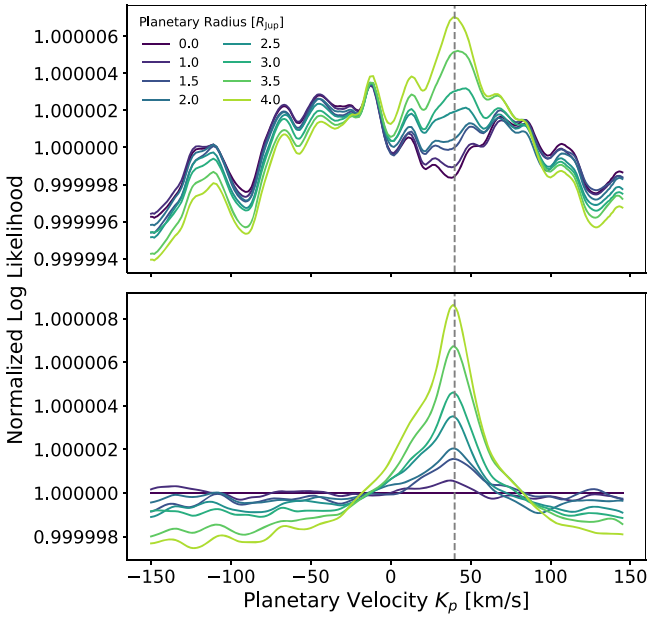

Figure 2. Simulated log-likelihood results showing the effects of increasing HD 88133 b planetary radius. These simulations approximate NIRSPEC1.0 L-band data taken with the same orbital phases (f) and primary velocities in the original data. The bottom panel shows the log-likelihood results with the structured noise curve ($R_{\rm pl} = 0$) subtracted off.

The stellar model used to generate and cross correlate the simulated data differs from the stellar model used to cross correlate the observed data in Piskorz et al. (2016) in how its continuum is removed. The stellar model used for cross correlation in Piskorz et al. (2016) was continuum corrected with a second order polynomial fit from 2.0 to 3.5 μm in wavenumber space, while the model used here is corrected with a third-order polynomial fit from 2.8 to 4.0 μm in wavenumber space. The method of stellar continuum correction actually has a large effect on the shape of the resulting log-likelihood curve; when the data are cross correlated with a stellar model corrected by a 3rd order polynomial fit from 2.8–4.0 μm in wavenumber space, the resulting log-likelihood curve much more closely resembles the simulated curves (e.g., in Figure 2). We use the third-order, 2.8–4.0 μm approach in our simulations because this continuum correction method was validated in allowing common structure to be seen in the data and simulated log likelihoods of HD187123b (Buzard et al. 2020). Further, this approach resulted in a flatter looking stellar spectral model, and one that found the known stellar velocities in each epoch of data with higher likelihoods. We do note, however, that the seemingly strong dependence of the final log-likelihood shape on the method of stellar model continuum correction is concerning and warrants deeper investigation.

3.2.2. Planetary-radius Simulations

Because there seems to be no clear peak at a positive K_p in Figure 1, we use simulations to see how much larger the planetary radius would have to be for its peak to be distinguishable. For these simulations, we set the K_p at 40 km s^{-1} and the stellar radius at 2.20 $R_\odot$ (Ment et al. 2018), and step the planetary radius up from 1 $R_{\rm Jup}$ to 4 $R_{\rm Jup}$ in increments of 0.5 $R_{\rm Jup}$. Figure 2 shows the results of these simulations in the top panel. In the bottom panel, we show the detections that could be made if all of the structured noise (e.g.,

Table 2
Gaussian Fits to HD88133 Planetary-radius Simulations

R_{pl} (R_{Jup})	K_p (kms^{-1})	ΔK_p (kms^{-1})	Peak Height (σ)	R^2
Without Star Subtraction				
1.0	33	10	−0.7	2.1×10^{-3}
1.5	−33	22	1.5	0.27
2.0	−30	22	1.6	0.26
2.5	4	43	2.3	0.34
3.0	16	44	2.1	0.43
3.5	28	40	3.3	0.58
4.0	29	37	5.2	0.67
With Star Subtraction				
1.0	35	10	3.2	0.39
1.5	40	22	7.5	0.87
2.0	36	17	10.2	0.87
2.5	34	20	19.9	0.95
3.0	36	20	35.9	0.96
3.5	37	23	24.2	0.96
4.0	35	24	25.1	0.95

Note. These simulations were all run with an input K_p of 40 km s^{-1}. Prior to fitting, these log-likelihood results are subtracted by the mean of their values from −150 to 0 km s^{-1}. The Gaussian model is initiated with a 40 km s^{-1} center and 10 km s^{-1} standard deviation. The Gaussian peak height is reported over σ, which is measured as the standard deviation of the log-likelihood structure more than $3\Delta K_p$ above or below the best-fit Gaussian center, where ΔK_p is the standard deviation of the best-fit Gaussian model.

the $R_{pl} = 0$ result) could be effectively removed from the results containing a planetary signal.

In this high-S/N-per-epoch regime, we expect the contribution from structured noise to far outway the contribution from random noise (Buzard et al. 2020; Finnerty et al. 2021). The similarity between different radius simulations shows that this is still the case.

To quantify the strength of these detection peaks, we fit each with a Gaussian model and report the parameters in Table 2. In the noncorrected versions, the Gaussian model does not fit within one standard deviation of the input K_p until the planetary radius reaches 2.5 R_{Jup}, and the peak does not exceed 3σuntil a radius of 3.5 R_{Jup}. Even at this large radius, the Gaussian model does not clearly distinguish the planetary peak from the structured noise, which can be seen in the Gaussian center offset, large Gaussian width, and relatively low R^2 value. Much more promising detections could be made if there were a way to effectively remove the structured noise from the log-likelihood results. Even at 1 R_{Jup}, HD 88133 b could have been detected in the data with a significance over 3σ. These simulations take a number of liberties, though, that are not yet applicable to real data. They consider no telluric contamination outside of pixels lost to saturated telluric absorption. They also assume that the stellar and planetary spectra in the data are perfectly matched to the stellar and planetary templates used for cross correlation. Thus, while the corrected simulations shown in the bottom panel of Figure 2 provide an optimistic view of the possible detections with the six particular NIRSPEC1.0 *L*-band epochs presented in Piskorz et al. (2016), the uncorrected versions give much more realistic estimates.

HD 88133 b has a minimum mass of 0.27 ± 0.01 M_{Jup} (Piskorz et al. 2016). With a radius of 3.5 R_{Jup}, it would have a minimum density of 0.01 g cm^{-3}. A growing classifcation of planets with exceptionally large radii for their masses, called "super-puffs," have low densities of $\lesssim$0.3 g/cm^3 (e.g., Cochran et al. 2011; Jontof-Hutter et al. 2014; Vissapragada et al. 2020). While HD 88133 b ($M_p \sin i \sim 85 M_\oplus$) is too massive to be classified as a super-puff ($M_p \lesssim 10$–$15 M_\oplus$, Piro & Vissapragada 2020), by comparison of its density, we can conclude that it is highly improbably the planet's radius would be as high as 3.5 R_{Jup}. Indeed, hot-Jupiter inflation can approach 2 R_{Jup} (Thorngren & Fortney 2018), but has not been observed to exceed it to this extent.

Our simulations therefore confirm that HD 88133 b is not detectable from the six *L*-band epochs of data presented in Piskorz et al. (2016). These radius simulations did, however, provide useful information in telling us that the planetary signal would need to be raised by about an order of magnitude (or the structured noise lowered by the same amount), to allow for a confident detection. We now turn to simulations to ask how that order of magnitude may be made up observationally rather than by altering parameters of the physical system like the planetary radius.

3.2.3. Upgraded NIRSPEC Simulations

The NIRSPEC instrument was upgraded in early 2019, after the Piskorz et al. (2016) publication. The upgrade would afford six usable *L*-band orders per echelle/cross disperser setting as opposed to the 4 from NIRSPEC1.0. It would give twice as many pixels per order (2048 versus 1024), a nearly doubled spectral resolution (∼41,000 versus 25,000), and a ∼40% larger wavelength coverage per order (Martin et al. 2018).

We run NIRSPEC2.0 simulations with the same orbital phases and primary velocities in the original six NIRSPEC1.0 epochs to determine whether the instrument upgrade would have given the planetary signal the boost it needed to be detectable. These simulations are generated as described in Section 3.2.1, with the following exceptions. The six orders per epoch cover roughly 2.9331–2.9887, 3.0496–3.1076, 3.1758–3.2364, 3.3132–3.3765, 3.4631–3.5292, and 3.6349–3.6962 μm. We broaden the simulated data to an average instrumental resolution of 41,000 and assume a S/N per pixel per epoch of 2860, or a total S/N per pixel of 7000 across the six epochs. The data wavelength axes, locations of saturated telluric pixels, and Gaussian kernals used to broaden the simulated data were taken from the 2019 April 3 and 2019 April 8 NIRSPEC2.0 data of HD187123 presented in Buzard et al. (2020).

Figure 3 shows the results of the simulations that imagine the HD88133 *L*-band epochs had been taken with the upgraded NIRSPEC instrument. In light purple is the simulation with no planetary signal added and in darker purple is the simulation with a 1 R_{Jup} planetary signal. While the likelihood at the input K_p of 40 km s^{-1} is increased from the corresponding no planet log likelihood, it does not form a peak and would not constitute a detection. The six *L*-band HD88133 epochs were positioned such that even with the upgraded instrument, they would not have enabled a planetary detection.

3.2.4. Near-zero Primary-velocity Simulations

Buzard et al. (2021) recently showed that, in the small epoch number limit, epochs taken when the primary velocity of a system is near zero are better at reducing structured noise and revealing planetary signatures than epochs taken during periods

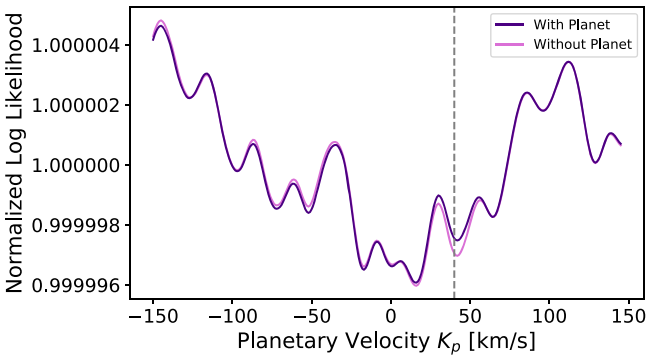

Figure 3. NIRSPEC2.0 simulation of HD 88133 b with same orbital phases (f) and primary velocities as in the original data. The data represented by the curve in dark purple has a 1 R_{Jup} planetary signal and the curve in light purple has no planetary signal.

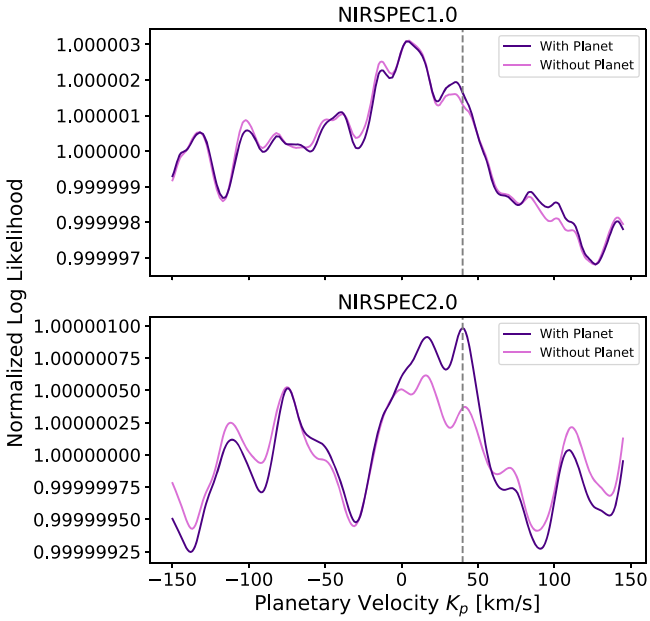

Figure 4. HD 88133 b simulations considering the orbital phases (f) from the six original L-band epochs, but with 0 km s^{-1} primary velocities. The top panel approximated NIRSPEC1.0 data and the bottom panel approximates NIRSPEC2.0 data.

with larger absolute primary velocities. The majority of the structured noise that arises in the simulations presented here and in Buzard et al. (2021) results from correlation between the planetary spectral template and the stellar component of the simulated data. We thus suspect that the reduction of structured noise at a primary velocity of zero relates to the portion of the stellar spectrum masked by saturated tellurics when there is a minimal velocity shift between the two spectra. It could be that at this velocity shift, the stellar features that most strongly correlate with the planetary template are masked by saturated tellurics, and without them, the structured noise level decreases substantially. One must be careful in applying this prediction, though, since a primary velocity of zero would bring not just the stellar spectrum, but also the planetary spectrum, closer to the telluric rest frame. While our simulations assume perfect correction of nonsaturated tellurics, any residual tellurics that make it through a correction routine could mask planetary features. In a small epoch number limit, an optimal routine might therefore include near-zero primary velocities (to reduce structured noise from star/planet correlation) and quadrature orbital positions (to maximize the planet/telluric velocity separation). With a much larger number of epochs, the structured noise from planet/star correlation may be reduced naturally by the many different combinations of primary and secondary velocities and the usefulness of near-zero primary velocity epochs may be lessened.

We can ask whether, with just the six epochs on HD88133, near-zero primary velocities might have helped. HD88133 has a primary velocity of zero twice a year: in late February and in mid-August. It would also be accessible from Keck in late February. For the following simulations, we assume epochs had been taken with the same orbital phases (f) as the original data, but in late February when $v_{\rm pri} = 0\,{\rm km\,s^{-1}}$. The original data epochs had primary velocities of 17.4, 18.1, 8.1, 16.2, 25.7, and 19.5 km s^{-1}. We run these simulations with both the NIRSPEC1.0 and NIRSPEC2.0 configurations.

Figure 4 shows the results of the 0 primary velocity simulations with NIRSPEC1.0 results in the top panel and NIRSPEC2.0 results in the bottom panel. In each, we show a pure structured noise simulation (light purple), or simulation with no planetary signal in the simulated data, so that the planetary peak in the simulation with the planetary signal (darker purple) can be distinguished from the structured noise.

We first consider the NIRSPEC1.0 simulation. While the 1 $R_{\rm Jup}$ planetary signal definitely shows a larger peak here than when analyzed with the original primary velocities (Figure 2), it still does not constitute a very strong detection. We can think of a number of reasons for this. Buzard et al. (2021) showed that near-zero primary velocity epochs could raise the detection significance on average ∼2–3× over random primary velocity epochs. From our radius simulations, we estimate an order of magnitude is needed. The gain from near-zero primary velocities then may not be sufficient. HD88133A has an effective temperature of 5438 K (Mortier et al. 2013), putting it on the cooler end of host stars considered by Buzard et al. (2021). Cooler host stars showed a stronger preference for near-zero primary-velocity epochs, which means, in this case, we might expect a bit more than a 3× increase. On the other hand, here, we consider a K_p of 40 km s^{-1}, smaller than the 75 km s^{-1} K_p used for most of the simulations in Buzard et al. (2021). A smaller K_p brings all of the secondary velocities closer in magnitude to the primary velocity; when the primary velocity is 0 km s^{-1}, the secondary velocities are closer to 0 km s^{-1} and the planetary spectrum is closer to the telluric rest frame. That the near-zero primary-velocity approach brings the planetary spectrum closer to the telluric frame when combined with a smaller K_p could detract from its advantage over a more random set of primary velocities. Regardless of how these factors work out, Figure 4 confirms that a near-zero primary-velocity observing strategy could not have made up for the order of magnitude needed for a strong detection of HD88133b with the orbital phases of the six L-band NIRSPEC1.0 epochs obtained and presented in Piskorz et al. (2016).

The simulations considering near-zero primary velocity epochs taken with the upgraded NIRSPEC instrument, shown in the bottom panel of Figure 4, show the most promising chance of detection. There is a peak centered at $K_p = 40\,{\rm km\,s^{-1}}$. A Gaussian fit to the simulated result (dark purple) with no prior information reports a measurement of $22 \pm 20\,{\rm km\,s^{-1}}$, with a height of 3.2σ. If this result were from real data, and we were able to assign the peak at ∼17 km s^{-1} to noise rather than the planetary signature through either fits with

Table 3
Ups And b Epoch Positions

Date	Piskorz et al. (2017)	This work	
	M	*M*	*f*
2011 Sep 6	1.54	1.33	1.36
2011 Sep 7	2.90	2.69	2.70
2011 Sep 9	5.45	5.24	5.21
2013 Oct 27	3.71	3.50	3.49
2013 Oct 29	0.13	6.20	6.20
2013 Nov 7	6.22	6.01	6.01
2014 Oct 7	1.99	1.78	1.81

simulations (e.g., Buzard et al. 2020) or because the planet had a radius inflated (e.g., Charbonneau et al. 2000) above the 1 R_{Jup} assumed here, we could expect a more refined fit.

4. Upsilon Andromedae b

Piskorz et al. (2017) reported the direct detection of upsilon Andromedae b at a K_p of 55 ± 9 km s^{-1} using seven epochs of Keck/NIRSPEC *L*-band data, three epochs of *K*-band data covering the left-hand side of the detector, and three *K*-band epochs covering the right-hand side of the detector. For this work, we will again just consider the *L*-band epochs.

4.1. Correction to Piskorz et al. (2017) Results

Piskorz et al. (2017) approximated the orbit of ups And b as circular, and so reported mean anomaly *M* values, rather than true anomaly *f* values, because they would be the same in the circular limit. We find, however, that there was a systematic error in the calculation of the secondary velocities that stemmed from a mismatch between the zero points used in Equations (3) and (2). This resulted in a net error comparable to mean anomalies roughly −3.3% offset from their true values. Table 3 lists the mean anomalies used in Piskorz et al. (2017) and the corrected anomalies measured from pericenter, calculated using orbital parameters from Wright et al. (2009).

Figure 5 shows how these offsets affect the resulting log-likelihood curve from the seven epochs of ups And NIRSPEC *L*-band data. The originally published log-likelihood curve is in red and is reproduced in black dashed. The corrected log-likelihood curves are shown in blue (eccentric orbit) and orange (circular orbit). As in the case of HD 88133 b, we can see here that for low eccentricity orbits, there is no benefit to considering an eccentric orbit rather than assuming a circular one.

4.2. Ups And Simulations

We were interested in running similar simulations to those run for HD88133 in Section 3.2 to see whether the peak at ∼55 km s^{-1} can be substantiated. We are particularly curious about whether we could expect the planetary peak to be as strong as it appears in Figure 5 since ups And, like HD88133, has a large stellar radius ($1.7053529^{+0.1024430}_{-0.0621246}$ $R_\odot$; Gaia Collaboration et al. 2018).

4.2.1. Generation of Simulated Data

We generate ups And simulated data as described in Section 3.2.1. For these simulations, we use a stellar model generated from the PHOENIX stellar model grid (Husser et al. 2013) interpolated to an effective temperature of 6213 K, a metallicity of 0.12, and a surface gravity of 4.25 (Valenti & Fischer 2005). We assume a stellar radius of 1.7053529 $R_\odot$ (Gaia Collaboration et al. 2018) and a planetary radius of 1.0 R_{Jup} unless otherwise stated. The simulated data are continuum corrected with a 3rd order polynomial fit from 2.8 to 4.0 μm in wavenumber space.

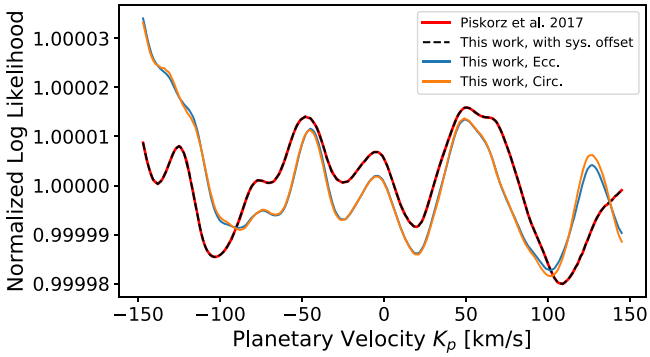

Figure 5. The normalized log-likelihood result for ups And b originally published in Piskorz et al. (2017) is shown in red. It is reproduced, in black dashed, by including a systematic offset in the epoch positions. The corrected log-likelihood curves are shown in blue (eccentric orbit) and orange (circular orbit).

We rotationally broaden the stellar model with a stellar rotation rate of 9.62 km s^{-1} (Valenti & Fischer 2005) and limb-darkening coefficient of 0.29 (Claret 2000). The FWHM of the instrumental kernels of NIRSPEC1.0 and NIRSPEC2.0 are about 12 and 7.3 km s^{-1}, respectively, so while rotational broadening makes little difference to data from NIRSPEC1.0, it would have a larger effect on data from the upgraded NIRSPEC instrument.

The stellar spectral model used to analyze the ups And *L*-band data in Piskorz et al. (2017) was not from the PHOENIX grid. Instead, they used a model similar to that described in Lockwood et al. (2014). It was generated from a recent version of the LTE line analysis code MOOG (Sneden 1973) and the MARCS grid of stellar atmospheres (Gustafsson et al. 2008). Notably, individual abundances were set by matching observed lines for elements that were well measured by NIRSPEC. While tests run on both Tau Boo and ups And NIRSPEC1.0 *L*-band data show that stellar models generated this way are able to measure the true stellar velocities at each epoch with higher likelihoods than PHOENIX stellar models, because these models are generated without a continuum, they cannot be used to generate simulated data. Further, because they rely on fits to NIRSPEC1.0 observational data, they could not be used to generate simulated data outside of the NIRSPEC1.0 order wavelengths. Therefore, we are limited to the PHOENIX stellar model.

We use a planetary model from the SCARLET planetary spectral modeling framework (Benneke 2015) without a thermal inversion. The planetary model used in the original work was also from the SCARLET framework, but did include a thermal inversion. We decide to run simulations with a noninverted planetary model because most recent hot-Jupiter atmospheric studies are finding noninverted thermal structures (e.g., Birkby et al. 2017; Piskorz et al. 2018; Pelletier et al. 2021).

We use orbital positions *f* from the final column of Table 3, Wright et al. (2009) orbital parameters, and a K_p of 55 km s^{-1} in Equation (2) to determine the secondary velocities at each

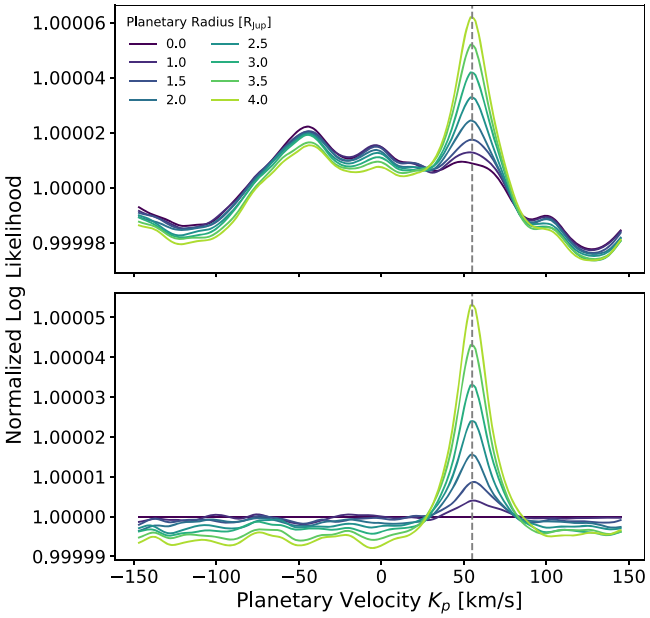

Figure 6. Ups And simulations showing the effects of increasing planetary radius. The simulations approximate NIRSPEC1.0 *L*-band data with the orbital phases (f) and primary velocities from the original seven epochs of data. The bottom panel shows each log-likelihood result with the structured noise curve ($R_{pl} = 0$) subtracted off.

epoch. The primary velocities at each epoch are −49.7, −49.4, −48.9, −30.5, −29.6, −25.4, and −39.2 km s^{-1}.

Gaussian noise is added at the level of the data (total S/N per pixel = 18192).

4.2.2. Planetary-radius Simulations

As for HD88133b, we first run simulations with an increasing planetary radius. Figure 6 shows the results of these simulations with the planetary radius increasing from 1.0 to 4.0 R_{Jup} in increments of 0.5 R_{Jup}. Table 4 report the parameters from Gaussian fits to the log-likelihood curves. While Gaussian models can reliably measure a peak centered around the input K_p, the R^2 values show that a Gaussian model would not be justified until at least a planetary radius of 3.5 to 4.0 R_{Jup}. While transiting hot Jupiters have been observed with radii approaching 2 R_{Jup} (e.g., KELT-26 b, Rodríguez Martínez et al. 2020), it is improbable that ups And b would have a radius larger than that. These simulations, therefore, do not suggest that, with a reasonable radius, ups And b could be well detected in the 7 original NIRSPEC1.0 *L*-band epochs.

4.2.3. Upgraded NIRSPEC Simulations

The ups And NIRSPEC2.0 simulations are set up the same way as the HD88133 NIRSPEC2.0 simulations with one exception. Because ups And ($K = 2.9$) is much brighter than HD88133 ($K = 6.2$), we assume a S/N per pixel per epoch of 9000, or a total S/N per pixel of 23800, across the seven epochs. At the average S/N of 6530 per pixel in the NIRSPEC1.0 data, we were already well into the regime where structured noise far outweighs white noise, so anything more should make little to no difference to the results.

Figure 7 shows a clear peak at the input K_p of 55 km s^{-1}. It does, coincidentally, fall at the same position as a structured noise peak (in light purple), suggesting that its significance could be overestimated. Any other value of K_p would result in a

Table 4
Gaussian Fits to Ups And Planetary-radius Simulations

R_{pl} (R_{Jup})	K_p (kms^{-1})	ΔK_p (kms^{-1})	Peak Height (σ)	R^2
Without Star Subtraction				
1.0	50	12	0.7	0.01
1.5	52	12	1.1	0.07
2.0	53	11	1.6	0.15
2.5	53	11	2.2	0.27
3.0	54	11	2.8	0.38
3.5	54	11	3.7	0.52
4.0	54	11	4.5	0.61
With Star Subtraction				
1.0	58	12	7.4	0.81
1.5	56	12	19.6	0.96
2.0	55	11	25.1	0.97
2.5	55	11	36.5	0.98
3.0	55	11	44.3	0.99
3.5	55	12	54.3	0.99
4.0	55	12	47.2	0.98

Note. These simulations were all run with an input K_p of 55 km s^{-1}. Prior to fitting, these log-likelihood results are subtracted by the mean of their values from −150 to 0 km s^{-1}. The Gaussian model is initiated with a 55 km s^{-1} center and 10 km s^{-1} standard deviation. The Gaussian peak height is reported over σ, which is measured as the standard deviation of the log-likelihood structure more than $3\Delta K_p$ above or below the best-fit Gaussian center, where ΔK_p is the standard deviation of the best-fit Gaussian model.

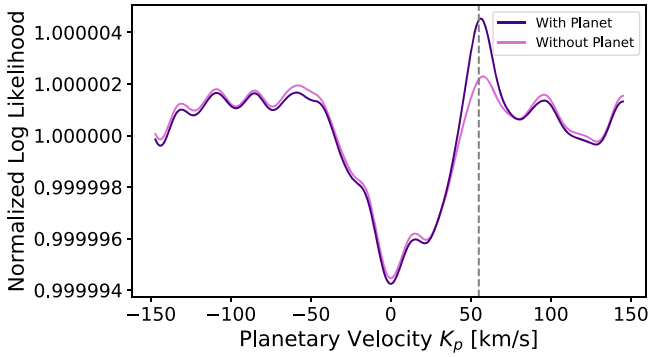

Figure 7. NIRSPEC2.0 simulation of ups And with the same orbital phases (f) and primary velocities as in the original data.

weaker peak that would need to be distinguished, through some mechanism, from the noise peak at ∼55 km s^{-1}. With the input K_p at 55 km s^{-1}, a Gaussian model reports a fit at 57 ± 7 km s^{-1} with a height of 2.1σ.

This result is encouraging in that it implies that NIRSPEC2.0 would have allowed a multiepoch detection of ups And b with the exact seven epochs presented in Piskorz et al. (2017) even with a planetary radius of 1 R_{Jup}.

4.2.4. Near-zero Primary-velocity Simulations

Because of its relatively large systematic velocity of −28.59 km s^{-1} (Nidever et al. 2002), ups And never reaches a primary velocity of 0 km s^{-1}. The nearest its primary velocity gets to zero is −2 km s^{-1} in late January/early February every year. During this time of year, it would be accessible from Keck during the first few hours of the night, setting, in early February, at around 7 UT. This would optimistically allow for an hour and a half on target after telescope focusing on a good night. Because ups And is a very bright source, enough S/N

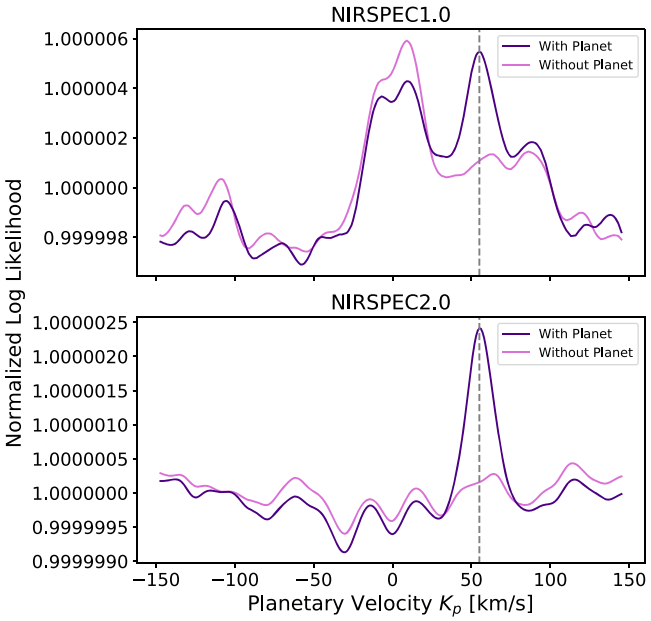

Figure 8. Ups And simulations with the same orbital phases (f) as the original data, but with primary velocities in each epoch equal to $-2\,\mathrm{km\,s^{-1}}$. The simulations in the top panel approximate NIRSPEC1.0 data and those in the bottom panel approximate NIRSPEC2.0 data.

could be achieved to enter the regime where structured noise, rather than random noise, dominates very quickly. PCA-based telluric correction approaches, like those used in Piskorz et al. (2016) and Piskorz et al. (2017), require enough observation time to witness variation in the telluric spectrum. We run the following simulations assuming that the time before ups And sets would be enough to witness telluric variation sufficient to be picked up by PCA or that the data could be well telluric corrected by another approach. Then, these simulations are run with either the NIRSPEC1.0 or NIRSPEC2.0 setup and with the same orbital phases (f) as were in the original data, but with primary velocities at each epoch of $-2\,\mathrm{km\,s^{-1}}$.

Figure 8 shows the results of these simulations with the NIRSPEC1.0 results in the top panel and the NIRSPEC2.0 results in the bottom panel. Both configurations show strong features at the input K_p values, with the NIRSPEC2.0 result especially strong and unaltered, in shape, by adjacent structured noise features. A Gaussian model reports a fit to the NIRSPEC2.0 result of $56 \pm 8\,\mathrm{km\,s^{-1}}$ with a height of 10.8σ. While the seven L-band epochs could have provided a confident planetary detection if taken with NIRSPEC2.0 as is, if they had been taken following the recommendations of Buzard et al. (2021), with near-zero primary velocities, they could have presented a very strong detection and a chance for further atmospheric characterization (e.g., Finnerty et al. 2021).

5. Discussion

In this work, we reevaluated the multiepoch detections of HD 88133 b (Piskorz et al. 2016) and ups And b (Piskorz et al. 2017), correcting for errors in the estimated orbital positions at the observation times. Unfortunately, we find that the data is insufficient to report planetary detections or measurements of K_p in either case. Multiepoch detections with small data sets have always been a risk; stellar RV measurements are now made with tens, if not hundreds, of epochs.

HD 88133 b and ups And b were two particularly difficult planets to target. Both orbit very large stars, resulting in planet-to-star contrasts lower than those of typical hot Jupiters. At high resolution, the planet/star photospheric contrast provides an upper bound for the spectroscopic information content and thus gives only a first check on how easily detectable planets may be. Predictions of the line-to-continuum, or spectroscopic, contrasts, which can be significantly lower than photospheric contrasts, would provide a more useful guide to direct detection studies. However, they are highly dependent on the nature of atmospheric chemistry, in particular whether hazes are present, and thermal structure, meaning that model predictions will have large uncertainties. Here we consider photospheric contrasts as a first glimpse into why the spectroscopic detections of HD 88133 b and ups And b may have been so elusive. Measuring photospheric contrast as the mean ratio of planetary flux to stellar flux across the L band, we estimate planet-to-star contrasts for HD 88133 b and ups And b as 2.3×10^{-4} and 2.5×10^{-4}, respectively, with an assumed radius of 1 $\mathrm{R_{Jup}}$ for each planet. By comparison, HD 187123 b, studied in Buzard et al. (2020), has an expected L-band contrast of 1.4×10^{-3} and Tau Boötis b, studied in Lockwood et al. (2014), has an expected contrast somewhere between 1.1–1.5 $\times 10^{-3}$, depending on whether or not water is included in its model spectrum (see Pelletier et al. 2021 for a discussion into water on Tau Boo b). Each of these planets has a contrast nearly an order of magnitude larger than do HD 88133 b and ups And b. Our radius simulations show that in each case, a planetary radius of $\gtrsim$3 $\mathrm{R_{Jup}}$ would have allowed for a strong detection. As planet-to-star contrast increases with $\mathrm{R_{pl}^2}$, a radius of 3 $\mathrm{R_{Jup}}$ would increase their contrasts nearly the order of magnitude needed to be comparable to HD 187123 b and Tau Boo b.

We considered whether the upgrade to the NIRSPEC instrument (Martin et al. 2018) or the near-zero primary-velocity observing strategy presented by Buzard et al. (2021) would have allowed for enough reduction in structured noise to reveal these low contrast signals. The combination of both would offer a stronger chance of detection in both cases. Near-zero primary-velocity epochs obtained with NIRSPEC2.0 would have allowed for K_p measurements of HD 88133 b as $22 \pm 20\,\mathrm{km\,s^{-1}}$ with a height of 3.2σ (input $K_p = 40\,\mathrm{km\,s^{-1}}$) and of ups And b as $56 \pm 8\,\mathrm{km\,s^{-1}}$ with a height of 10.8σ (input $K_p = 55\,\mathrm{km\,s^{-1}}$). Several factors could explain why ups And b could be much more strongly detected under these conditions. It was observed with seven epochs while HD 88133 b was observed with six. Additionally, while both stars have large radii, ups And A is not quite as large as HD 88133 A (1.7053529 versus 2.20 $R_\odot$). Perhaps most importantly, ups And A has a higher effective temperature than HD 88133 A (6213 versus 5438 K). The cooler a stellar effective temperature, the more complex its spectrum will be. Therefore, HD 88133 A would have a more complex spectrum that would allow for more correlation between the stellar component of the data and the planetary spectral model used for cross correlation that gives rise to the structured noise in the final log-likelihood results. Additionally, ups And A not only has a less complex spectrum, but also one that is rotationally broadened. The stellar rotational broadening would also work to lessen the degree of correlation between the planetary model and the stellar component of the data. A smaller factor could be the total S/N. Ups And is a much brighter system, and so was simulated with a higher total S/N of 238000 compared to 7000

for HD88133b. Both cases are in a regime where structured noise outweighs white noise, though, so this is not likely a major contributor. Collectively, these factors all work to make ups And b more easily detectable than HD 88133 b. Though, even ups And b was below the detection limit with a small number of NIRSPEC1.0 *L*-band epochs.

The upgrade to the NIRSPEC instrument will provide a significant advantage to multiepoch planetary detection, due to its increases in both resolution and spectral grasp (Finnerty et al. 2021). However, in these difficult cases, it might be worthwhile to consider new observational approaches altogether. Since white noise does not appear to be the limiting factor in these multiepoch studies, we could consider an observational campaign on a smaller telescope (for example, UKIRT) that could dedicate more nights to this work. Another approach could be to consider an instrument like IGRINS or GMTNIRS which could simultaneously afford both a higher spectral resolution than NIRSPEC and a wider wavelength coverage, both of which are beneficial for planet detectability (Finnerty et al. 2021). Many of these instruments are optimized for shorter wavelengths ($<2.5\ \mu$m) than we have observed with NIRSPEC. As such, careful work into the optimal observing strategies as well as instrument settings will be crucial in the multiepoch approach's journey beyond NIRSPEC.

Ultimately, we want to stress the importance of using simulations in multiepoch work. Simulations are essential for understanding the origin and structure of the expected noise in high resolution data, considering both white noise and any structured noise that may arise in cross-correlation space. They can offer realistic estimates for the overall sensitivity of the data beyond expectations from a shot noise limit. As such, simulations can and should be used in many ways, e.g., for planning observations (e.g., Buzard et al. 2021), for identifying and reducing sources of structured noise (Buzard et al. 2020), and for evaluating approaches of atmospheric characterization (e.g., Finnerty et al. 2021).

Despite its challenges, the NIRSPEC multiepoch approach has been used to characterize planetary atmospheric structure. Piskorz et al. (2018) combined the multiepoch detection of KELT-2A b with Spitzer secondary eclipse data. They found that the multiepoch data provided roughly the same constraints on metallicity and carbon-to-oxygen ratio as the secondary eclipse data. Further, while the secondary eclipse data provided a stronger constraint on f, the stellar incident flux which is a rough measure of energy redistribution, the multiepoch data constrained it to low values, with a 50% confidence interval at 1.26. As models with $f \gtrsim 1.5$ show a temperature inversion, this indicates that using NIRSPEC1.0 multiepoch data alone, Piskorz et al. (2018) were able to determine that KELT-2A b has a noninverted thermal structure in the regions probed by $\sim 3\ \mu$m data. Finnerty et al. (2021) used NIRSPEC2.0 *L*-band simulations to look more deeply into the atmospheric constraints that could be made with multiepoch data and found that warm Jupiters' ($T_{\rm eq} \sim 900$ K) carbon-to-oxygen ratios could be constrained enough to differentiate between substellar, stellar, and superstellar values. While planetary detection using the multiepoch approach can a challenging pursuit, once the true planetary peak has been identified, the approach holds potential for detailed atmospheric characterization.

6. Conclusion

In this work, we present and correct errors in the multiepoch detections of HD 88133 b (Piskorz et al. 2016) and ups And b (Piskorz et al. 2017). Unfortunately, we find that the original NIRSPEC1.0 *L*-band data presented (six epochs for HD 88133 b, seven for ups And b) are insufficient for planetary detections. We run simulations to determine what would have been required for confident detections. Ups And b could have been strongly detected (10.8σ) if its seven *L*-band epochs had been taken with the upgraded NIRSPEC instrument and following the near-zero primary-velocity observing strategy presented by Buzard et al. (2021). HD 88133 b would be more difficult to detect, because of its larger stellar radius and lower stellar effective temperature, and would likely have required more, carefully planned, data.

This has been a very difficult result to discover and to publish. C.B. wants to acknowledge D.P.'s mentorship. D.P. is an incredible scientist and researcher, and C.B.'s journey through graduate school would not have been possible without the support so generously given. As Judith Butler wrote, "There was and remains warrant ... to distinguish between self-criticism that promises a more democratic and inclusive life for the movement and criticism that seeks to undermine it altogether." We hope this publication falls into the former category and promises a more democratic and inclusive life for the multiepoch cross-correlation approach moving forward.

We want to acknowledge Katie Kaufman's contribution to the ups And NIRSPEC data reduction along with support from NASA XRP grant NNX16AI14G. We thank our anonymous reviewer for their kind and close reading of our manuscript.

ORCID iDs

Cam Buzard https://orcid.org/0000-0002-9943-6124
Danielle Piskorz https://orcid.org/0000-0003-4451-2342
Geoffrey Blake https://orcid.org/0000-0003-0787-1610
Travis S. Barman https://orcid.org/0000-0002-7129-3002
Björn Benneke https://orcid.org/0000-0001-5578-1498
Chad F. Bender https://orcid.org/0000-0003-4384-7220
John S. Carr https://orcid.org/0000-0002-6695-3977

References

Beatty, T. G., Pepper, J., Siverd, R. J., et al. 2012, ApJL, 756, L39
Benneke, B. 2015, arXiv:1504.07655
Birkby, J. L., de Kok, R. J., Brogi, M., Schwarz, H., & Snellen, I. A. G. 2017, AJ, 153, 138
Brogi, M., Giacobbe, P., Guilluy, G., et al. 2018, A&A, 615, A16
Brogi, M., & Line, M. R. 2019, AJ, 157, 114
Brogi, M., Snellen, I. A. G., de Kok, R. J., et al. 2012, Natur, 486, 502
Bryan, M. L., Knutson, H. A., Howard, A. W., et al. 2016, ApJ, 821, 89
Butler, R. P., Wright, J. T., Marcy, G. W., et al. 2006, ApJ, 646, 505
Buzard, C., Finnerty, L., Piskorz, D., et al. 2020, AJ, 160, 1
Buzard, C., Pelletier, S., Piskorz, D., Benneke, B., & Blake, G. A. 2021, AJ, 162, 26
Charbonneau, D., Brown, T. M., Latham, D. W., & Mayor, M. 2000, ApJL, 529, L45
Claret, A. 2000, A&A, 363, 1081
Cochran, W. D., Fabrycky, D. C., Torres, G., et al. 2011, ApJS, 197, 7
Finnerty, L., Buzard, C., Pelletier, S., et al. 2021, AJ, 161, 104
Fischer, D. A., Laughlin, G., Butler, P., et al. 2005, ApJ, 620, 481
Fulton, B. J., Petigura, E. A., Blunt, S., & Sinukoff, E. 2018, PASP, 130, 044504
Gaia Collaboration, Brown, A. G. A., Vallenari, A., et al. 2018, A&A, 616, A1
Guilluy, G., Sozzetti, A., Brogi, M., et al. 2019, A&A, 625, A107
Gustafsson, B., Edvardsson, B., Eriksson, K., et al. 2008, A&A, 486, 951

Husser, T. O., Wende-von Berg, S., Dreizler, S., et al. 2013, A&A, 553, A6
Jontof-Hutter, D., Lissauer, J. J., Rowe, J. F., & Fabrycky, D. C. 2014, ApJ, 785, 15
Lockwood, A. C., Johnson, J. A., Bender, C. F., et al. 2014, ApJL, 783, L29
Martin, E. C., Fitzgerald, M. P., McLean, I. S., et al. 2018, Proc. SPIE, 10702, 107020A
Ment, K., Fischer, D. A., Bakos, G., Howard, A. W., & Isaacson, H. 2018, AJ, 156, 213
Mortier, A., Santos, N. C., Sousa, S. G., et al. 2013, A&A, 557, A70
Murray, C. D., & Dermott, S. F. 1999, Solar System Dynamics (Cambridge: Cambridge Univ. Press)
Nidever, D. L., Marcy, G. W., Butler, R. P., Fischer, D. A., & Vogt, S. S. 2002, ApJS, 141, 503
Nugroho, S. K., Kawahara, H., Masuda, K., et al. 2017, AJ, 154, 221
Pelletier, S., Benneke, B., Darveau-Bernier, A., et al. 2021, AJ, 162, 73
Piro, A. L., & Vissapragada, S. 2020, AJ, 159, 131
Piskorz, D., Benneke, B., Crockett, N. R., et al. 2016, ApJ, 832, 131
Piskorz, D., Benneke, B., Crockett, N. R., et al. 2017, AJ, 154, 78
Piskorz, D., Buzard, C., Line, M. R., et al. 2018, AJ, 156, 133
Rodríguez Martínez, R., Gaudi, B. S., Rodriguez, J. E., et al. 2020, AJ, 160, 111
Sneden, C. 1973, ApJ, 184, 839
Snellen, I. A. G., Brandl, B. R., de Kok, R. J., et al. 2014, Natur, 509, 63
Snellen, I. A. G., de Kok, R. J., de Mooij, E. J. W., & Albrecht, S. 2010, Natur, 465, 1049
Thorngren, D. P., & Fortney, J. J. 2018, AJ, 155, 214
Valenti, J. A., & Fischer, D. A. 2005, ApJS, 159, 141
Vissapragada, S., Jontof-Hutter, D., Shporer, A., et al. 2020, AJ, 159, 108
Wright, J. T., Upadhyay, S., Marcy, G. W., et al. 2009, ApJ, 693, 1084
Zucker, S. 2003, MNRAS, 342, 1291